Automatic Segmentation of SAR imagery Using Mixture Models

Zahra Jafari [1,2*], Pradeep Bobby [1,2], Rocky Taylor[1], and Ebrahim Karami [1]

[1] Faculty of Engineering and Applied Sciences, Memorial University, St. John's, NL A1B 3X7, Canada;
[2] C-CORE, St. John's, NL A1B 3X5, Canada
* Correspondence: zjafari@mun.ca

Keywords: SAR, Iceberg detection, segmentation, Gamma mixture models, Lognormal mixture models, Rayleigh Mixture Model.

Abstract
Synthetic Aperture Radar (SAR) image segmentation underpins target detection, land cover classification, and environmental monitoring, yet remains challenging due to speckle, non-Gaussian backscatter statistics, and outliers. This paper presents a comparative evaluation of mixture-model–based segmentation tailored to SAR, with a focus on Radarsat Constellation Mission (RCM) imagery. We propose a segmentation algorithm that selects one of three statistical mixture models—Rayleigh, Gamma, or Lognormal—to model SAR backscatter and produce soft (posterior) segmentations, followed by posterior thresholding and optional MRF-ICM post-processing to enhance spatial coherence and suppress speckle-induced errors. We compare against standard operational approaches, threshold-based methods (CFAR, multi-threshold Otsu) and conventional mixture-model labeling that designates the largest-scale component as the target.

On RCM data, the Rayleigh Mixture Model (RMM) is the strongest: at target pixels, the posterior probability of the largest-mean component is typically very close to 1, allowing a single Rayleigh component to capture the main body of the iceberg reliably. Unlike threshold-based baselines that yield hard segmentations, our Mixture Model (MM) approach outputs soft posteriors, enabling principled HH/HV fusion and downstream machine learning (ML). These results underscore the promise of RMM for robust iceberg detection; future work will integrate Rayleigh-based posterior features with lightweight ML classifiers to further improve performance across sensors and conditions.

1. Introduction

Synthetic Aperture Radar (SAR) provides day–night, all-weather imaging capabilities that are indispensable for maritime operational safety, ship transit monitoring, and environmental surveillance. Segmenting SAR imagery into semantically meaningful regions (e.g., open water, sea ice, icebergs) is a crucial prerequisite for downstream tasks such as target detection and tracking, ice charting, and coastal hazard assessment. Accurate segmentation of icebergs and sea ice not only supports safe navigation and maritime operations but also contributes to situational awareness in dynamic and potentially hazardous environments [Jafari et al., 2023].

However, accurate segmentation remains challenging due to the presence of multiplicative speckle noise, non-Gaussian and scene-dependent backscatter statistics [Goodman, 1963], and heterogeneous scattering mechanisms (surface, volume, and double-bounce) that produce pixel-level mixtures. These difficulties are further amplified at higher incidence angles and in operational maritime environments characterized by variable sea states and clutter [Shi et al., 2023].

Recent deep learning–based approaches, such as CNN, U-Net, and Transformer variants, achieve strong supervised results by learning hierarchical features directly from data [Chen, 2021; Noori et al., 2025; Jafari et al., 2025]. However, they require large labeled datasets, are computationally intensive, and may be sensitive to errors in training annotations and variations in sensor configurations or environmental conditions, limiting their robustness in operational scenarios. In contrast, statistical mixture models are statistically transparent, grounded in the physical principles of SAR backscatter, and fully unsupervised, offering better adaptability across sensors and imaging configurations [Gao, 2010; Oliver, 2004]. Mixture models are particularly suited to SAR imagery because backscatter intensity arises from multiple scattering mechanisms with distinct statistical signatures whose parameters depend on dielectric properties, surface roughness, and spatial homogeneity.

Parametric models tailored to multiplicative speckle have therefore been widely adopted, including the Gamma distribution for multi-look intensity, the Rayleigh distribution for single-look amplitude, the Lognormal distribution as a computationally efficient empirical alternative under moderate heterogeneity, and the Gaussian distribution in the logarithmic (dB) domain, where log-intensity approximates Gaussian behavior [Moser et al., 2006; Xie et al., 2002; Ling et al., 2023]. Extending these single-component distributions to mixtures enables unsupervised, multi-modal segmentation using the Expectation–Maximization (EM) algorithm [[Celeux & Govaert, 1992; Doulgeris, 2015; Qin, 2023]. Mixture models naturally capture the multi-peaked intensity distributions nature of SAR backscatter, allowing the segmentation algorithm to account for heterogeneous pixels that combine surface, volume, and double-bounce scattering mechanisms.

Two traditional thresholding methods are often used in operational practice. The Constant False Alarm Rate (CFAR) detector performs adaptive thresholding with explicit control of the false-alarm rate by modeling local clutter statistics, whereas Otsu's method is distribution-agnostic and determines thresholds directly from image histograms. Neither method explicitly exploits SAR-specific spatial or statistical structure, and both are typically applied after despeckling to reduce the local variance of statistics. Consequently, their performance degrades in heterogeneous or multi-class scenes, and they do not provide a probabilistic framework for soft segmentation or uncertainty quantification [Færch et al., 2023; Xu et al., 2020].

Despite extensive prior work on SAR segmentation, there remains a lack of controlled performance evaluations specifically focused on maritime target extraction using mixture-model–

This contribution has been peer-reviewed. The double-blind peer-review was conducted on the basis of the full paper.
https://doi.org/10.5194/isprs-annals-XI-M-1-2026-11-2026 | © Author(s) 2026. CC BY 4.0 License.

based segmentation algorithms on current-generation C-band SAR constellations dataset (the Radarsat Constellation Mission (RCM) and Sentinel-1). This study addresses this gap by benchmarking three mixture families—Rayleigh, Gamma, and Lognormal—against traditional methods (Otsu and CFAR) for iceberg segmentation in open-water and sea-ice scenes. Performance is assessed qualitatively through visual inspection, focusing on the accurate delineation of homogeneous regions, accurately capturing target-background interfaces, and consistency across varying sea and imaging conditions. The results provide practical guidance on the most suitable statistical assumptions for C-band SAR iceberg detection and boundary extraction.

The remainder of this paper is organized as follows: Section 2 describes the datasets and regions of interest used in this study; Section 3 details the proposed methodology; Section 4 presents the experimental results and discussion; and Section 5 concludes the paper with final remarks.

2. Data

2.1 Dataset and Study Area

This study utilized two distinct Synthetic SAR datasets to rigorously evaluate the performance and generalization capabilities of the proposed iceberg detection framework. Both datasets cover the east coast of Canada, a region characterized by significant iceberg activity and dynamic ice conditions, making it an area of high operational interest.

The primary dataset comprises dual-polarized (HH, HV) imagery acquired by the RCM. Key system specifications for RCM are detailed in *Table 1*. These RCM scenes were strategically selected to encompass a wide range of seasonal ice conditions, from stable winter pack ice to melting summer sea ice, ensuring a comprehensive assessment of the detection framework's adaptability. Ground truth labeling for these scenes was meticulously performed using a combination of multi-sensor reference data, including Sentinel-1 SAR, Sentinel-2 optical imagery, and corroborated by auxiliary ship and iceberg reports, thereby providing robust and reliable validation.

For analysis, imagery was partitioned into 100×100-pixel (2 km×2 km) patches and processed with a Lee despeckling filter to reduce local variance. To ensure a robust performance evaluation, patches were categorized into calm open water, windy open water, and sea ice based on digital ice charts [Canadian Ice Service, 2009]. This framework benchmarks the ability of statistical mixture models to accurately perform iceberg shape estimation while maintaining edge definition across varying sea states

For cross-sensor validation, a secondary dataset consisting of Sentinel-1 dual-polarized (HH, HV) imagery was included in the analysis. These scenes, also from the same Canadian east coast region, allowed for an assessment of the method's transferability and robustness when applied to a different SAR system. While Sentinel-1 shares similar C-band characteristics with RCM, it presents different levels of radiometric uncertainty and variations in spatial resolution (*Table 1*). To maintain comparability, only Sentinel-1 scenes that spatially overlapped with the RCM study area were included in this dataset. The geographic coverage of both datasets is illustrated in *Figure 1*.

Sensor	Mode / Product	Spacing / Resolution (m)	Looks (R×A)	SW (km)	NESZ (dB)	Pol
RCM	MR (50 m) / GRD	20 / ~50	4×1	350	−22	HH, HV
S-1	IW / GRD	40 / ~20×40	5×1	400	−25	HH, HV

Table 1. key specifications of the SAR datasets used in this study.

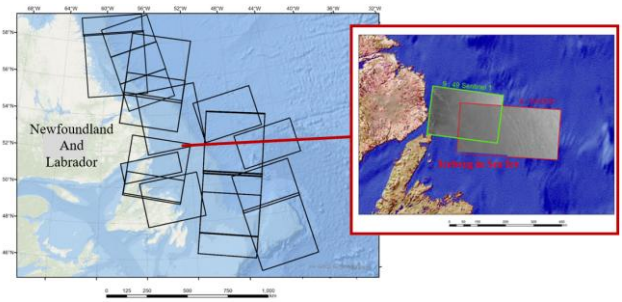

Figure 1. Geographic and SAR data coverage of the datasets used in this study.

2.2 Data Analysis

In this subsection, we analyze the distribution of homogeneous 100×100-pixel SAR patches corresponding to Calm Water, Windy Water, and First-Year Ice by fitting three statistical distributions: Lognormal, Rayleigh, and Gamma. The fitted distributions, overlaid on the patch histograms, are depicted in *Figure 2* and *Figure 3* for HH and HV polarizations, respectively, and the corresponding fitting errors and correlations are summarized in *Table 2* and *Table 3*.

For HH polarization, all surface types are best described by the Lognormal distribution, as indicated by the lowest MSE and KS statistics in *Table 2* . For HV polarization**,** the Lognormal distribution consistently provides the best fit across all surface types (*Table 3*). The histograms in Figure 3 confirm that the σ^0 in HV polarization is approximately Gaussian for all surfaces, which explains the superior fit of the Lognormal distribution.

These results demonstrate that the choice of statistical model depends on both polarization and surface type. HH and HV polarization can be effectively described using a single Lognormal model. This finding is critical for subsequent SAR image analysis, including sea ice segmentation and iceberg detection, where accurate statistical modeling of the amplitude distribution is essential for reliable classification.

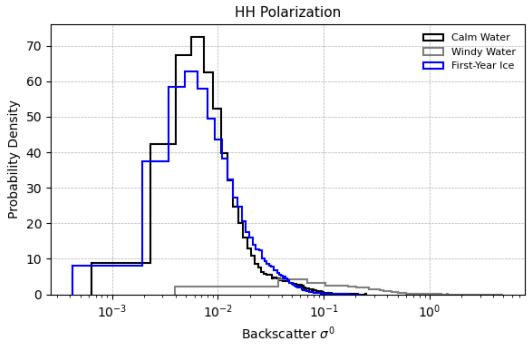

Figure 2. Histogram of HH-polarized SAR amplitude distributions for 100x100-pixels different surface types (Calm Water, Windy Water, and First-Year Ice).

Surface	Distribution	MSE	Correlation	KS Stat	KS P-value
Calm Water	**Lognormal**	**5.67**	0.9806	**0.057**	9.69×10^{-14}
	Rayleigh	69.20	0.7102	0.267	0.0
	Gamma	33.12	0.8703	0.112	0.0
Windy Water	**Lognormal**	**0.015**	**0.9828**	**0.049**	**8.21×10^{-10}**
	Rayleigh	0.055	0.9246	0.116	0.0
	Gamma	0.096	0.9115	0.319	0.0
First-Year Ice	**Lognormal**	**0.511**	0.9980	**0.016**	7.04×10^{-13}
	Rayleigh	41.43	0.8289	0.190	0.0
	Gamma	95.02	0.5632	0.422	0.0

Table 2. Goodness-of-fit metrics for HH polarization SAR amplitudes. The best-fitting distribution for each surface type is highlighted in bold.

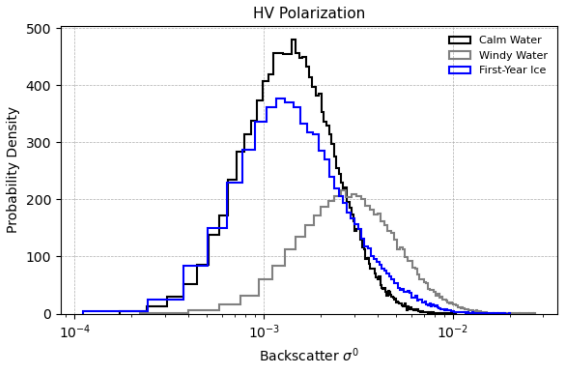

Figure 3. Histogram of HV-polarized SAR amplitude distributions for 100x100-pixels different surface types (Calm Water, Windy Water, and First-Year Ice).

Surface	Distribution	MSE	Correlation	KS Stat	KS P-value
Calm Water	**Lognormal**	**254.42**	0.9941	**0.02**	2.26×10^{-21}
	Rayleigh	1243.5	0.9703	0.07	2.80×10^{-21}
	Gamma	28467.27	0.0976	0.54	0.0
Winy Water	**Lognormal**	**3.60**	0.9995	**0.00**	1.31×10^{-12}
	Rayleigh	279.86	0.9631	0.08	0.0
	Gamma	4626.82	0.1715	0.50	0.0
First-Year Ice	**Lognormal**	**16.92**	0.9990	**0.00**	9.62×10^{-41}
	Rayleigh	1706.79	0.8989	0.14	0.0
	Gamma	9551.14	0.2552	0.51	0.0

Table 3. Goodness-of-fit metrics for HV polarization SAR amplitudes. The best-fitting distribution for each surface type is highlighted in bold.

3. Methodology

In this section, three mixture models are described. For each method, the mathematical formulation and associated parameters are presented. These parameters are iteratively estimated using the Expectation-Maximization (EM) [Celeux & Govaert, 1992] algorithm.

3.1 Mixture Models for SAR Intensities

Let I_i denote the intensity of pixel i, and K the number of mixture components (classes). A general mixture model can be expressed as [McLachlan & Peel, 2000]:

$$p(I_i) = \sum_{k=1}^{K} \pi_k^{(m)} f_m\left(I_i \middle| \theta_k^{(m)}\right), \mathrm{m} \in \{\mathrm{Ray},\ \mathrm{Gamma},\ \mathrm{LN}\}$$

Where

- $f_m\left(I_i \middle| \theta_k^{(m)}\right)$ is the probability density function of the k-th component for model m,
- $\theta_k^{(m)}$ is the set of parameters for component k of model m,
- $\pi_k^{(m)}$ is the mixing weight, with $\sum_{k=1}^{k} \pi_k^{(m)} = 1$.

The posterior probability that pixel i belongs to class k is:

$$p(L_i = k|I_i) = \frac{\pi_k^{(m)} f_m\left(I_i \middle| \theta_k^{(m)}\right)}{\sum_{j=1}^{K} \pi_j^{(m)} f_m\left(I_i \middle| \theta_j^{(m)}\right)}$$

The parameters $\{\pi_k^{(m)}, \theta_k^{(m)}\}$are iteratively estimated using the EM algorithm until convergence.

For the specific distributions considered in this work:

Model m	Density $f_m\left(I_i \middle\| \theta_k^{(m)}\right)$	Parameters $\theta_k^{(m)}$
Rayleigh	$\frac{I_i}{\sigma_k^2} exp\left(-\frac{I_i^2}{2\sigma_k^2}\right),\ I_i \geq 0$	$\sigma_{k\ (scale)}$
Gamma	$\frac{\beta_k^{a_k}}{\mathrm{r}(a_k)} I_i^{a_k-1} exp(-I_i\beta_k)\ ,\ I_i \geq 0$	σ_k, β_k(shape,rate)
Lognormal	$\frac{1}{\sqrt{2\pi} I_i \sigma_k} exp\left[-\frac{(\ln I_i - \mu_k)^2}{2\sigma_k^2}\right],\ I_i > 0$	μ_k, σ_k(mean, std of log-intensity)

3.2 Segmentation algorithm

The algorithm employed in this study (*Table 4*) integrates statistical mixture modeling with spatial regularization to segment icebergs in SAR imagery. A three-component mixture model is adopted for each 100 × 100-pixel patch (~2 km × 2 km), where the components correspond to three classes defined based on prior knowledge of the scene: background (calm or windy open water, or sea ice), intermediate backscatter (e.g., target

boundaries or mixed pixels), and high-backscatter targets (e.g., icebergs or ships).

The mixture model is fitted using the EM algorithm, producing posterior probabilities for each pixel. The components are ordered according to their scale parameter, which reflects the variability of backscatter intensity (e.g., σ_k for Rayleigh or the mean for Lognormal). The largest-scale component is designated as the target class when present.

To extract the final detections, a high-confidence posterior threshold (≥0.99) is applied to the target component. This step reduces false positives, particularly at target-background interfaces and within shadowed regions, ensuring the model captures the main body of the iceberg with high precision. To further refine the output, spatial consistency is enforced using a Markov Random Field with Iterated Conditional Modes (MRF-ICM) [Geman & Geman, 1993; Boykov et al., 2002; Ružić et al., 2012]. This optimization enforces spatial label consistency among neighbouring pixels, which mitigates speckle-induced 'salt-and-pepper' noise and produces spatially coherent iceberg masks that are structurally consistent and robust

Input:	**I: SAR intensity image; K=3 components; posterior_threshold=0.99; smoothness_weight; Model: RMM, GaMM, or LMM**
Output:	L: segmentation map; T: binary iceberg mask
1:	Initialize mixture parameters using k-means on log-transformed intensity
2:	repeat // EM Algorithm
3:	Compute posterior probabilities for each pixel and component
4:	Update mixture weights and component parameters
5:	until convergence
6:	Sort components by σ_k(in RMM) , mean(in GaMM), and μ (in LMM)low to high; assign highest scale as target class
7:	Assign initial labels using maximum posterior; detect targets with posterior >= 0.99
8:	repeat // ICM Spatial Regularization
9:	Update each pixel label to minimize energy (data term + neighbor smoothness)
10:	until no label changes
11:	Update final target mask from regularized labels; return L, T

Table 4. Proposed Algorithm.

across varying sea states.

4. Results and Discussion

In this section, we first report standard maximum-posterior labelling results using three mixture models (Rayleigh, Gamma, Lognormal), followed by results from our proposed mixture-model algorithm with posterior thresholding and MRF-ICM regularization. Experiments are conducted on 100 × 100 RCM patches from HH and HV polarization channels across three scene types: calm open water, windy open water, and sea ice.

4.1 Comparison of baseline mixture-model–based segmentation

Figure 4 presents standard mixture-model–based segmentation results, where the component with the largest-mean component is labeled as the target. In HH, the RMM reliably delineates iceberg boundaries and fine structures better than the GaMM and LMM models. In HV, although target details are effectively resolved, shadow regions are frequently misclassified as targets,

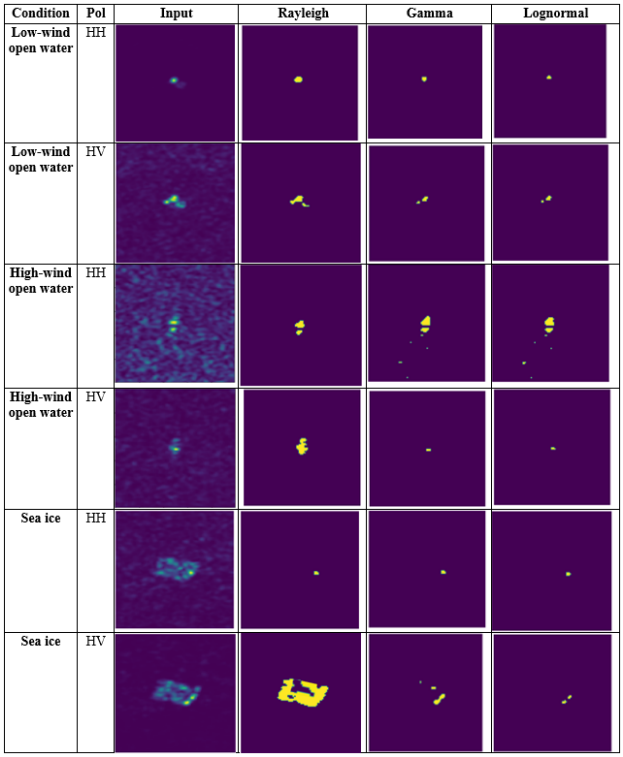

Figure 4. baseline mixture-model–based segmentation results (GaMM, LMM, RMM) for icebergs in calm open water, windy open water, and sea ice (HH and HV polarizations). RMM shows finer target structure in HH, but HV exhibits shadow-induced false positives, particularly in sea ice.

especially when the iceberg is embedded within sea ice. These observations are evident in all evaluated scene types, including calm open water, windy open water, and sea-ice scenes.

4.2 Performance of the proposed Segmentation Algorithm Using Mixture Models

In this section, we evaluate the proposed segmentation pipeline—comprising posterior-thresholded assignment of the largest-mean component followed by MRF-ICM—on 100×100 patches extracted from the HH and HV polarization channels. The data used for this evaluation are from SAR images acquired in two different transmit-receive polarization combinations for an iceberg observed in a high-wind open-water scene. The evaluation uses RMM, GaMM, and LMM mixtures, with results illustrated in *Figure 5*, 6, and 7, respectively. In each figure, panels (a) and (e) show the original HH and HV patches; panels (b) and (f) present the posterior probabilities of the dominant-class labels, which is equivalent to baseline mixture- model–based segmentation.

Panels (c) and (g) display the binary masks after applying a high-confidence posterior threshold of 0.99 to extract regions with relatively pure distributions that are most likely to represent targets. Finally, panels (d) and (h) overlay the MRF-ICM smoothed detections on the SAR images for visual interpretation. *Figure 5* presents the results obtained using the RMM. As shown, the proposed algorithm before thresholding provides soft labeling, which yields more probabilistic evidence compared to the standard maximum-posterior labeling shown in *Figure 4*. In panels (c) and (g), after applying the posterior probability threshold, only the pixels belonging to the target are highlighted. *Figure 6* shows the results using the GaMM. The outcome for the HH channel is similar to the baseline results in *Figure 4*; however, in the HV channel, a greater number of pixels are

labeled as targets. *Figure 7* presents the results obtained with the LMM. The segmentation results before thresholding contain more false positives compared to the previous two models; however, after thresholding, the results become comparable to those of the Gamma model. Overall, applying posterior thresholding prior to MRF-ICM smoothing effectively reduces false positives while preserving target structure, particularly in HH scenes when using LMM. The soft-labeling results indicate that when RMM is used, pixels more likely to correspond to targets exhibit posterior probabilities close to 1, while false positives and boundary regions have lower probabilities. In contrast, GaMM and LMM tend to produce more "hard" labeling, where most pixels have posterior probabilities near either 0 or 1. This performance trend suggests that the proposed algorithm using RMM has greater potential to be integrated with machine learning algorithms after feature extraction, compared to the other two models.

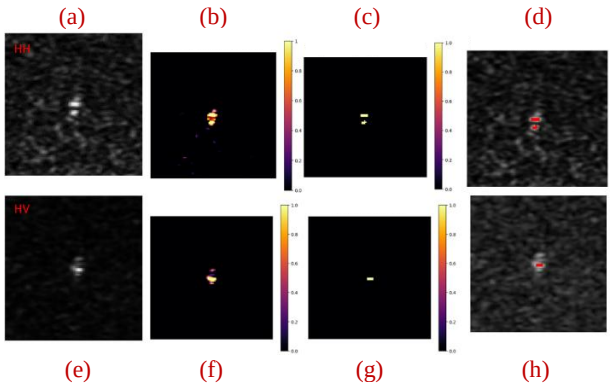

Figure 5. Iceberg segmentation pipeline using the RMM for a high-wind open-water scene. Panels (a) and (e) show the original HH and HV SAR patches. Panels (b) and (f) represent the soft labeling via posterior probabilities of the dominant target class. Panels (c) and (g) illustrate the binary target masks extracted using a 0.99 posterior probability threshold. Finally, panels (d) and (h) show the MRF-ICM refined detections overlaid on the original SAR imagery.

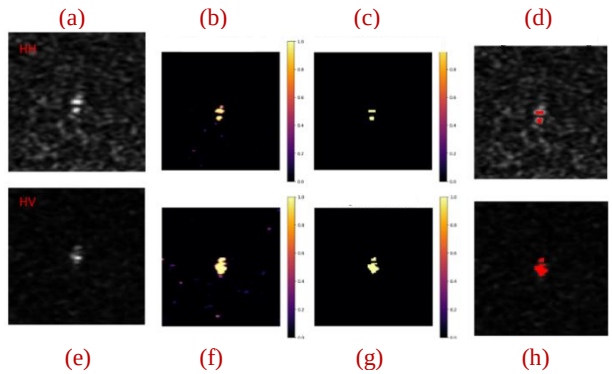

Figure 6. Iceberg segmentation pipeline using the GaMM for a high-wind open-water scene. Panels (a) and (e) show the original HH and HV SAR patches. Panels (b) and (f) depict the posterior probabilities of the dominant target class. Panels (c) and (g) show the binary masks produced by applying the 0.99 posterior threshold. Panels (d) and (h) display the final MRF-ICM smoothed detections overlaid on the imagery for visual comparison.

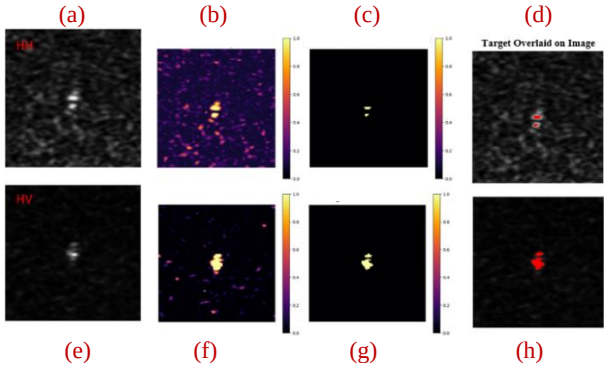

Figure 7. Iceberg segmentation pipeline using the LMM for a high-wind open-water scene. Panels (a) and (e) show the input HH and HV SAR imagery. Panels (b) and (f) present the soft posterior probabilities, while panels (c) and (g) display the binary masks after applying the 0.99 confidence threshold. Panels (d) and (h) show the spatially regularized detections after MRF-ICM post-processing, overlaid on the original patches

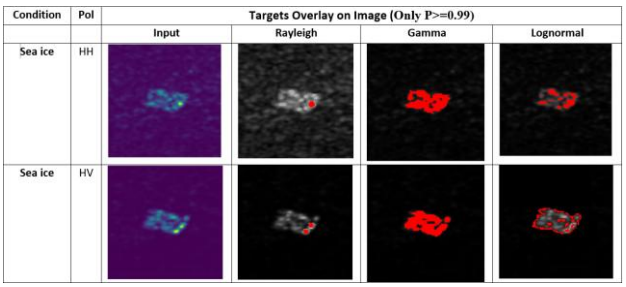

Figure 8. Final detection results for an iceberg embedded in thick first-year ice across three mixture models for the HH and HV polarization channels. All detections were generated by applying a 0.99 posterior threshold to the largest-mean component and are overlaid on the original SAR imagery for visual comparison

Figure 8 focuses on a highly challenging operational scenario: an iceberg embedded within thick first-year sea ice. The results present the final detections—obtained by applying a $P \geq 0.99$ threshold to the largest-mean component—overlaid on patches extracted from the HH and HV polarization channels. The RMM reliably delineates cleaner and more concise target masks, with fewer shadow-driven false positives, in both polarization channels. In contrast, the GaMM and LMM misclassify adjacent sea-ice regions as targets in both HH and HV.

4.3 Large RCM Scene Evaluation in Sea Ice: Proposed Method vs. Otsu's method and CFAR

In this section, we evaluate the proposed segmentation method using RMM, GaMM, and LMM against two baseline methods: CFAR (PFA = 10^{-5}) and Otsu's method (3 classes). *Figure 9* , the first image from the left presents HH channel of the region of interest—a large RCM scene (2000 × 2000 pixels, ~40 km × 40 km) from the east coast of Newfoundland and Labrador—containing multiple icebergs and broken sea ice embedded in thick first year sea ice. The baseline results demonstrate that Otsu's method, as a global thresholding approach, under-segments low-contrast icebergs and is sensitive to intensity imbalance, while CFAR provides adaptive background suppression but tends to over-detect targets in heterogeneous sea-ice textures. The proposed pipeline identifies targets based on the largest-mean mixture component, applies a high-confidence posterior threshold (≥ 0.99), and refines labels with MRF-ICM The performance of the proposed pipeline is benchmarked using

the RMM, GaMM, and LMM (see *Figure 10-12.*). The proposed RMM-based approach produces more spatially coherent iceberg masks with fewer false positives, effectively preserving target extent and boundaries. Qualitative assessment confirms its improved discrimination of iceberg bodies from the surrounding sea ice. In contrast, the proposed methods using GaMM and LMM tend to missclasify targets within sea-ice regions, with LMM performing the worst in this regard by producing more false positives than GaMM. The 250 pixels detected by the RMM represent a more realistic target count for the icebergs in the scene, whereas the 53k and 219k counts from GaMM and LMM indicate extensive misclassification of the surrounding sea-ice textures as target pixels. (see *Table 5*)

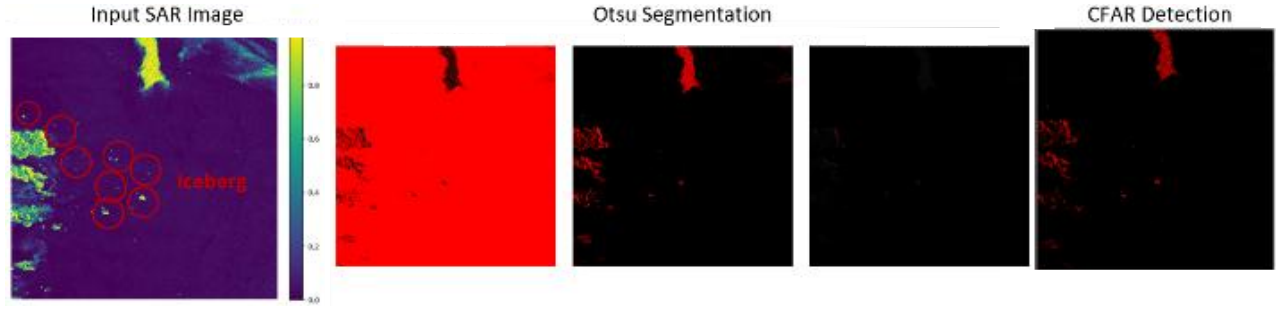

Figure 9. Evaluation of baseline segmentation methods on a large RCM sea-ice scene. Panel (a) shows the original HH SAR imagery. Panels (b–d) present results from Otsu's method using three classes: Class 0 (low-backscatter open water), Class 1 (sea ice), and Class 2 (high-backscatter targets). Panels (e) illustrate the CFAR detection results with a PFA= 10 −5.

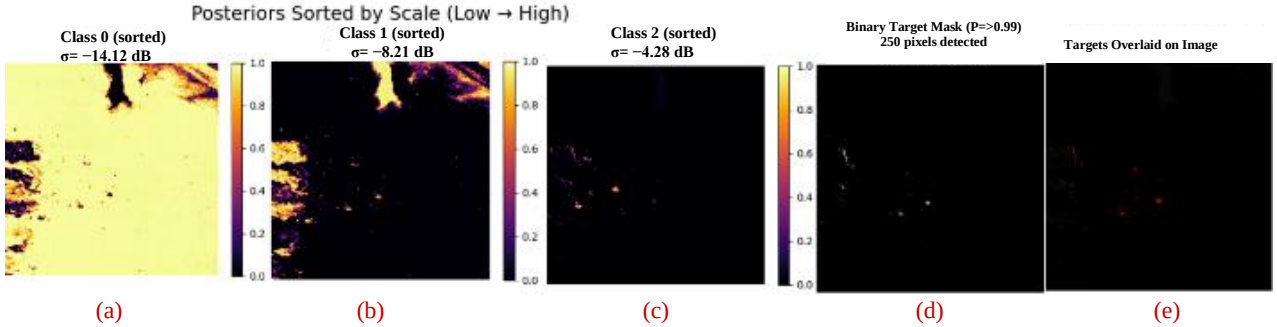

Figure 10. Segmentation results obtained by applying the RMM-based pipeline to the RCM scene. Panels (a–c) display the posterior probabilities for each class, sorted by the scale parameter from low to high. Panel (d) shows the binary target mask (P≥ 0.99), and panel (e) presents these detections overlaid on the original imagery.

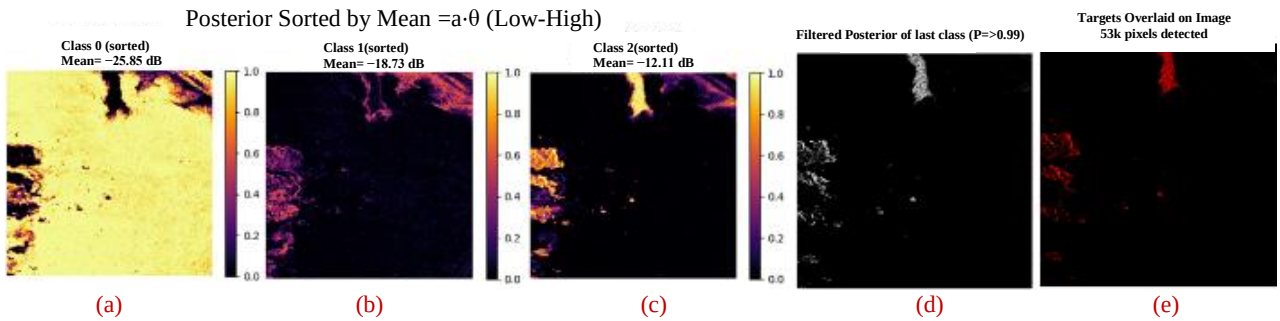

Figure 11. Segmentation results obtained by applying the GaMM -based pipeline to the RCM scene. Panels (a–c) display the posterior probabilities for each class, sorted by the mean parameter from low to high. Panel (d) shows the binary target mask (P≥0.99), and panel (e) presents these detections overlaid on the original imagery.

This contribution has been peer-reviewed. The double-blind peer-review was conducted on the basis of the full paper.
https://doi.org/10.5194/isprs-annals-XI-M-1-2026-11-2026 | © Author(s) 2026. CC BY 4.0 License.

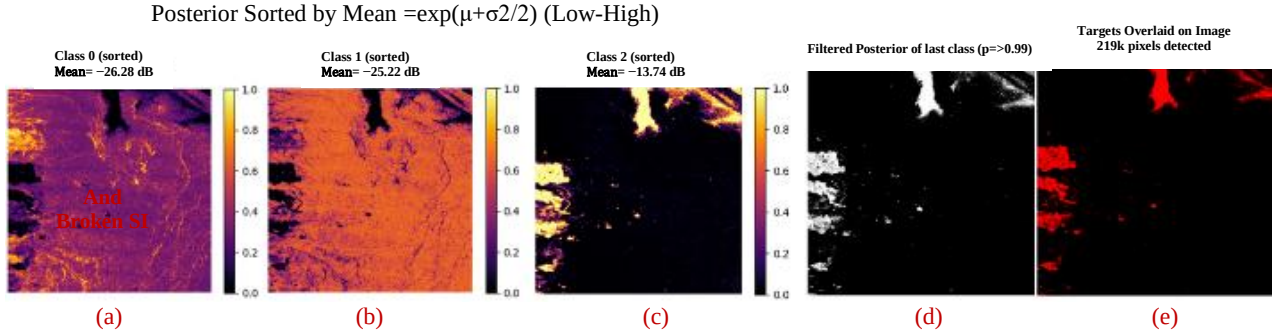

Figure 12. Segmentation results obtained by applying the LMM -based pipeline to the RCM scene. Panels (a–c) display the posterior probabilities for each class, sorted by the mean parameter from low to high. Panel (d) shows the binary target mask (P≥0.99), and panel (e) presents these detections overlaid on the original imagery.

Method	Mixture Model	Total Pixels Detected (*P*≥0.99)	Qualitative Observation
Proposed Pipeline	**RMM**	**250**	**Cleaner masks; minimal sea-ice false positives**
Proposed Pipeline	GaMM	53,000	Over-labels broken sea ice as targets
Proposed Pipeline	LMM	219,000	Significant false positives across sea-ice regions

Table 5. Comparison of target detection counts (pixels) for the 2000×2000 RCM scene.

4.4. Large Sentinel-1 Scene Evaluation in Sea Ice: Proposed Method vs. CFAR and Otsu's method

In this section, we evaluate the proposed segmentation method on a large Sentinel-1 scene (2000×2000 pixels, corresponding to 80 km × 80 km) from East Greenland (left side image in) This scene has coarser spatial resolution than RCM imagery and contains numerous icebergs embedded within thick, high-concentration multiyear sea ice partially covered by frost flower. The proposed pipeline identifies targets based on the highest-mean mixture component, applies a high-confidence posterior probability threshold (P ≥ 0.99), and refines the segmentation using MRF-ICM post-processing. To ensure comparability with RCM, the Sentinel-1 Digital Number (DN) values were converted to Sigma-Nought (σ^0) during the pre-processing stage

We compare the performance of three mixture models—Rayleigh, Gamma, and Lognormal against two traditional methods: CFAR (with PFA = 10^{-5}) and Otsu's method (3 classes). As shown in *Figure 13* . CFAR failed to detect any targets, likely due to small difference between background and target in this region. Otsu's method, despite being a global method, achieved a better performance than mixture models with initial threshold of 0.99; however, RMM outperform other algorithms including Otsu algorithm, when its threshold is optimized.

Figure 14 presents the segmentation results obtained using the proposed algorithm with the RMM. The model was initially configured with three components; however, the third class contained no valid data, as the mixture model failed to converge, and was therefore excluded from further analysis. By selecting the second component and applying a relaxed posterior probability threshold of P = 0.1, the model identified 227,027 potential target pixels, as shown in the binary mask (third column). The final column displays the detected targets (in red) overlaid on the original SAR image. With this adjustment, the proposed method demonstrates superior detection performance compared to Otsu's method.

Figure 15 illustrates the segmentation results obtained using the GaMM, where the posterior threshold was relaxed to p = 0.93 for the third component and the model identified 180,184 pixels as targets. Note that this threshold was set empirically as lower thresholds resulted in much more false positives than the ones we can see in the image.

Similarly, as one can see from *Figure 16,* the meaningful results when the threshold is lowered to 0.92. With this setting using LMM, the number of detected pixels, including false positives, was considerably higher than that of the RMM and GaMM models, with approximately 257,310 pixels identified as targets. This suggests that in multi-year highly concentrated sea ice environments, the posterior probabilities from mixture models may not exhibit sufficient separation between target and background classes, necessitating lower confidence thresholds and fewer mixture components for practical target detection. (See *Table 6*)

This contribution has been peer-reviewed. The double-blind peer-review was conducted on the basis of the full paper.
https://doi.org/10.5194/isprs-annals-XI-M-1-2026-11-2026 | © Author(s) 2026. CC BY 4.0 License.

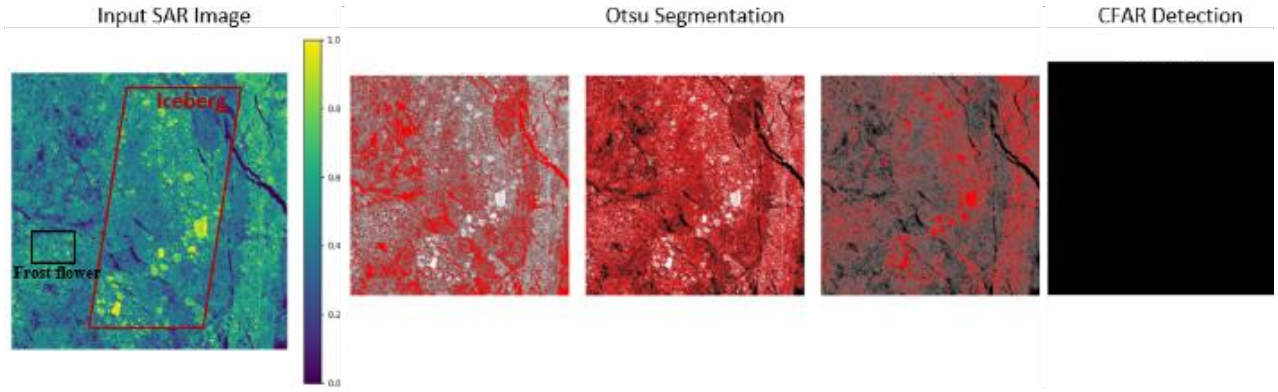

Figure 13. Evaluation of traditional segmentation methods on a large Sentinel-1 scene of a sea-ice region containing multiple icebergs and frost flowers. Panel (a) shows the original HH SAR imagery. Panels (b–d) present results from Otsu's method using three classes: Class 0 (low-backscatter open water), Class 1 (sea ice), and Class 2 (high-backscatter targets). Panels (e) illustrate the CFAR detection results with a PFA= 10^{-5}.

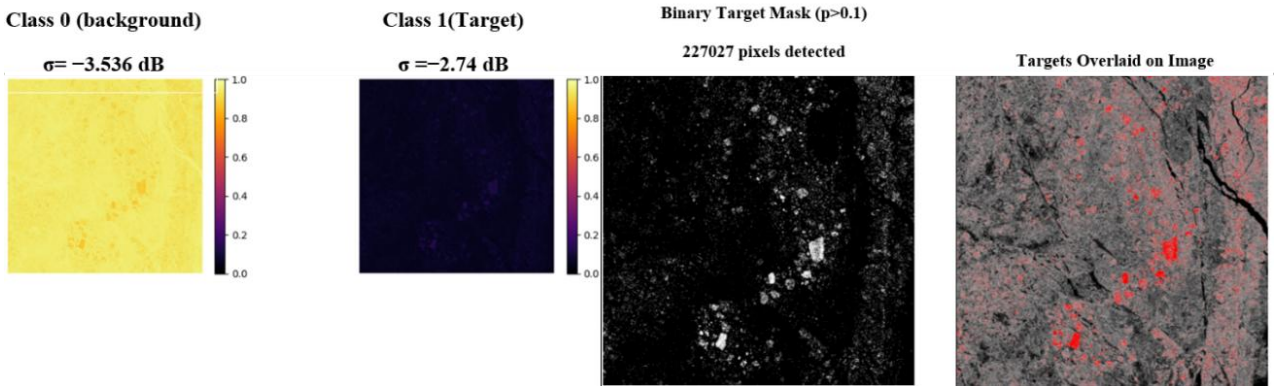

Figure 14. Segmentation results obtained by applying the proposed RMM pipeline to a Sentinel-1 scene. Panel (a) shows the input SAR imagery. While the model was initially configured with three mixture components, the third class did not effectively resolve the target pixels. Panel (b) presents the posterior probabilities for the target class. Panel (c) illustrates the binary target mask resulting from an adjusted posterior threshold (P>0.1). Panel (d) displays the detections overlaid on the original imagery for visual inspection.

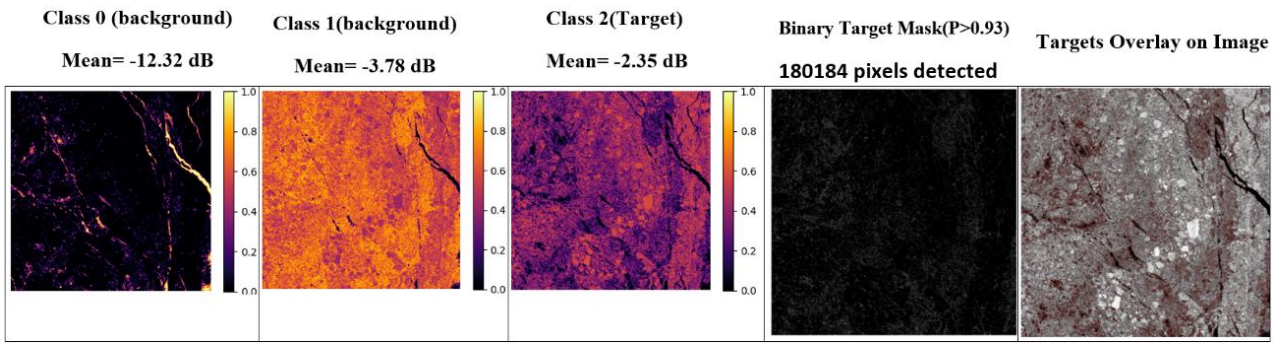

Figure 15. Segmentation results obtained by applying the GaMM-based pipeline to a large Sentinel-1 scene. Panel (a-c) presents the sorted three components based on mean values, the largest-mean component was specifically selected to represent the target class. Panel (d) illustrates the binary target mask obtained after applying a relaxed posterior threshold (P>0.93). Panel (c) displays these detections overlaid on the original imagery for qualitative assessment.

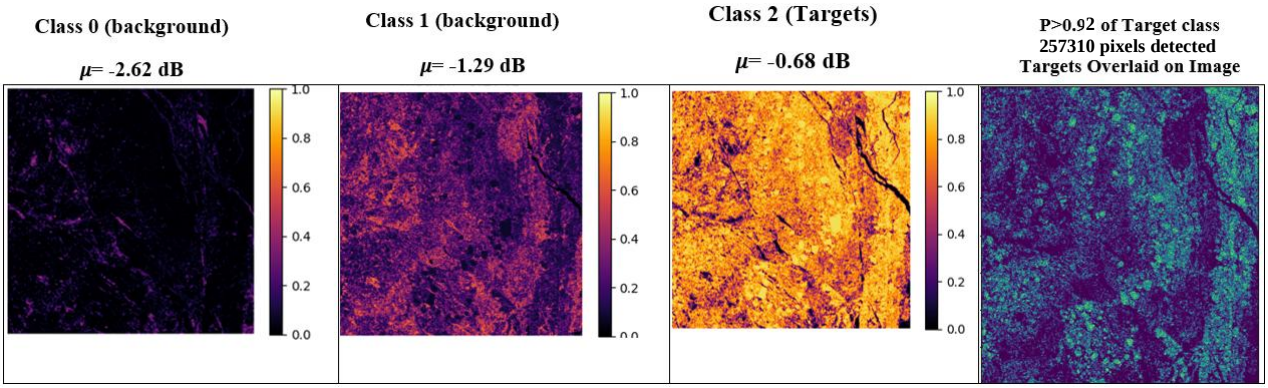

Figure 16. Segmentation results obtained by applying the LMM-based pipeline to a large Sentinel-1 scene Panel (a-c) presents the sorted three components based on mean values, the largest-mean component was specifically selected to represent the target class. Due to insufficient statistical separation between target and background classes in this environment, a relaxed posterior threshold of P>0.92 was applied to the largest-mean component. Panel (d) illustrates the resulting binary target mask.

Method	Mixture Model	Total Pixels Detected	Qualitative Observation
Proposed Pipeline	RMM	227,027 (***P*≥0.1**)	Mixture model failed to converge well
Proposed Pipeline	**GaMM**	**180,184 (*P*≥0.93)**	**Cleaner masks; minimal sea-ice false positives**
Proposed Pipeline	LMM	257,310 (***P*≥0.92**)	Significant false positives across sea-ice regions

Table 6. Comparison of target detection counts (pixels) for the 2000×2000 Sentinel-1 scene.

Acknowledgements

The authors would like to thank the Canadian Space Agency (CSA) for providing the Radarsat Constellation Mission (RCM) imagery and the European Space Agency (ESA) for the Sentinel-1 data. RCM Data © Government of Canada (2023); RADARSAT Constellation Mission Imagery © Canadian Space Agency. Sentinel-1 imagery contains modified Copernicus Sentinel data , processed by ESA.This research was undertaken thanks in part to funding from the Canada First Research Excellence Fund and Equinor Ltd.

5. Conclusion

This paper investigated statistical model–based segmentation and target detection in open water and sea ice using RCM in Sigma Naught(σ^0) imagery as the primary dataset, with additional validation on coarser-resolution Sentinel-1 scene. The proposed algorithm fit Rayleigh, Gamma, and Lognormal mixtures, assigned targets to the highest-mean component, applied posterior thresholding, and optionally refined labels with MRF-ICM. We compared against CFAR and Otsu's method on large-scene images. Across RCM scenes, the Rayleigh mixture model (RMM) consistently delivered stronger practical iceberg detection, and performed competitively alongside the other mixture models.

Unlike standard maximum-posterior labelling, threshold-based methods (CFAR, Otsu) that produce hard segmentations, our mixture-model (MM) approach yields soft segmentations via posterior probabilities. These posteriors enable principled fusion across polarization channels (e.g., HH and HV), and can be integrated into machine learning (ML) models to improve robustness and generalization. Among the MMs, Rayleigh is particularly well-suited for speckle-dominated targets, offering a simple, stable, and physically grounded representation with interpretable posteriors that complement multiple polarizations. Accordingly, future work will integrate Rayleigh-based posterior features with mathematically simpler alternative ML classifiers to jointly exploit HH and HV soft evidence and enhance detection performance across sensors and conditions.

References

Boykov, Y., Veksler, O., and Zabih, R., 2002. Fast approximate energy minimization via graph cuts. *IEEE Transactions on Pattern Analysis and Machine Intelligence*, 23(11), pp. 1222-1239.

Canadian Ice Service. (2009). Canadian Ice Service Arctic Regional Sea Ice Charts in SIGRID-3 Format. (G02171, Version 1. Date accessed 04-06-2026.

Celeux, G. and Govaert, G., 1992. A classification EM algorithm for clustering and two stochastic versions. *Computational Statistics & Data Analysis*, 14(3), pp. 315-332.

Chen, X., Su, N., Huang, Y., and Guan, J., 2021. False-alarm-controllable radar detection for marine target based on multi features fusion via CNNs. *IEEE Sensors Journal*, 21(7), pp. 9099-9111.

Doulgeris, A. P., 2014. An Automatic U-Distribution and Markov Random Field Segmentation Algorithm for PolSAR Images. *IEEE Transactions on Geoscience and Remote Sensing*, 53(4), pp. 1819-1827.

Færch, L., Dierking, W., Hughes, N., and Doulgeris, A. P., 2023. A comparison of CFAR object detection algorithms for iceberg identification in L-and C-band SAR imagery of the Labrador sea. *The Cryosphere Discussions*, 2023, pp. 1-26.

Gao, G., 2010. Statistical modeling of SAR images: A survey. *Sensors*, 10(1), pp. 775-795.

Geman, S. and Geman, D., 1993. Stochastic relaxation, Gibbs distributions and the Bayesian restoration of images. *Journal of Applied Statistics*, 20(5-6), pp. 25-62.

Goodman, N. R., 1963. Statistical analysis based on a certain multivariate complex Gaussian distribution (an introduction). *The Annals of Mathematical Statistics*, 34(1), pp. 152-177.

Jafari, Z., Karami, E., Taylor, R., and Bobby, P., 2023. Enhanced ship/iceberg classification in SAR images using feature extraction and the fusion of machine learning algorithms. *Remote Sensing*, 15(21), 5202.

Jafari, Z., Bobby, P., Karami, E., and Taylor, R., 2025. Automated Detection of Icebergs in the North Atlantic Using RCM Dual-Polarimetric SAR Imagery for Offshore Safety. *In International Conference on Offshore Mechanics and Arctic Engineering*, Vol. 88902, p. V001T02A019. American Society of Mechanical Engineers.

Ling, J., Wei, S., Gamba, P., Liu, R., and Zhang, H., 2023. Advancing SAR monitoring of urban impervious surface with a new polarimetric scattering mixture analysis approach. *International Journal of Applied Earth Observation and Geoinformation*, 124, 103541.

McLachlan, G.J, Peel D. Finite mixture models. *John Wiley & Sons*; 2000 Oct 2.

Moser, G., Zerubia, J., and Serpico, S. B., 2006. SAR amplitude probability density function estimation based on a generalized Gaussian model. *IEEE Transactions on Image Processing*, 15(6), pp. 1429-1442.

Noori, A. M., Ziboon, A. R., and AL-Hameedawi, A. N., 2025. Deep-learning integration of CNN–Transformer and U-net for bi-temporal SAR flash-flood detection. *Applied Sciences*, 15(14), 7770.

Oliver, C. and Quegan, S., 2004. *Understanding Synthetic Aperture Radar Images*. SciTech Publishing.

Qin, J., Liu, Z., Ran, L., Xie, R., Tang, J., and Zhu, H., 2023. An SAR image automatic target recognition method based on the scattering parameter Gaussian mixture model. *Remote Sensing*, 15(15), 3800.

Ružić, T., Pižurica, A., Philips, W. Neighborhood-consensus message passing as a framework for generalized iterated conditional expectations. *Pattern Recognition Letters*. 2012 Feb 1;33(3):309-18.

Shi, X., Wang, Y., You, H., and Chen, J., 2023. Sea Ice Extraction in SAR Images via a Spatially Constrained Gamma Mixture Model. *Sustainability*, 15(13), 10374.

Xie, H., Pierce, L. E., and Ulaby, F. T., 2002. Statistical properties of logarithmically transformed speckle. *IEEE Transactions on Geoscience and Remote Sensing*, 40(3), pp. 721-727.

Xu, S., Liao, Y., Yan, X., and Zhang, G., 2020. Change detection in SAR images based on iterative Otsu. *European Journal of Remote Sensing*, 53(1), pp. 331-339.